Journal of The
Electrochemical Society

OPEN ACCESS

# Simulation-Assisted Design of an Analytical Flow Cell for Industrially Relevant Performance Studies

To cite this article: C. Gohlke *et al* 2025 *J. Electrochem. Soc.* **172** 126501

View the article online for updates and enhancements.

You may also like

- Theoretical Insights into Equilibrium Potentials in Electrochemical Cells with Multiple Mobile Charge Carriers
Felix Ehrlich, Akhil Ashar, Oscar Furst et al.

- Electrolyte Motion–Induced Salt Inhomogeneity (EMSI) Can Occur Across Cell Formats: A Mechanistic Study in Single-layer Pouch Cells and Mitigation Strategies
Hao-Chen Hsiao, Daniel Goldbach, Jiahao Li et al.

- Design Optimization of Expanded Metal Mesh Flow Fields for Proton Exchange Membrane Water Electrolyzers
Nausir Mahmoud Firas and Iryna V. Zenyuk

Your Lab in a Box!

EL-CELL®
electrochemical test equipment

The PAT-Tester-i-16 Multi-Channel Potentiostat for Battery Material Testing!

✓ All-in-One Solution with Integrated Temperature Chamber (+10 to +80 °C)!
No additional devices are required to measure at a stable ambient temperature.

✓ Fully Featured Multi-Channel Potentiostat / Galvanostat / EIS!
Up to 16 independent battery test channels, no multiplexing.

✓ Ideally Suited for High-Precision Coulometry!
Measure with excellent accuracy and signal-to-noise ratio.

✓ Small Footprint, Easy to Setup and Operate!
Cableless connection of 3-electrode battery test cells. Powerful EL-Software included.

Learn more on our product website:
Scan me!

Download the data sheet (PDF):
Scan me!

Or contact us directly:
☎ +49 40 79012-734
✉ sales@el-cell.com
🌐 www.el-cell.com

This content was downloaded from IP address 134.94.123.71 on 19/01/2026 at 11:25

*Journal of The Electrochemical Society*, 2025 **172** 126501

# Simulation-Assisted Design of an Analytical Flow Cell for Industrially Relevant Performance Studies

**C. Gohlke,**[1,=] **C. Marcks,**[1,=,z] **V. Seidl,**[1] **M. Padligur,**[2] **and A. K. Mechler**[1,3,4,z]

[1] *Electrochemical Reaction Engineering (AVT.ERT), RWTH Aachen University, 52074 Aachen, Germany*
[2] *Chemical Process Engineering (AVT.CVT), RWTH Aachen University, 52074 Aachen, Germany*
[3] *Institute of Energy Technologies - Electrochemical Process Engineering (IET-4), Forschungszentrum Jülich, 52425 Jülich, Germany*
[4] *JARA-ENERGY, 52074 Aachen, Germany*

Electrochemical energy conversions require highly active and stable electrocatalysts. The development of such catalysts often occurs in academia, but the transition to industrial applications remains challenging. To study the activity and stability of electrocatalysts under more industrially relevant conditions, we designed an electrochemical flow cell (EFC) with 1 $cm^2$ parallel electrodes compatible with downstream analysis. Precise activity determination over a wide potential range and minimal dilution of reaction products with a restricted volume flow are ensured by a small reaction volume over the working electrode and by minimizing the inhomogeneities of mass transport of reactive species. Thereby, the influence of the reactive species' mass transport on the precision of the activity determination can be neglected. To evaluate this, we modeled the flow velocity distribution, concentration distribution, and particle flux of the reactive species over the electrode surface for different designs with COMSOL Multiphysics. The activity determination *via* the Koutecký-Levich analysis for the final EFC was simulated and experimentally validated. By coupling the EFC to online electrolyte analysis, the Fe concentration was successfully monitored during cyclic voltammetry and constant current operation at 10 mA $cm^{-2}$ with a $Ni_{70}Fe_{30}$ anode in 1 M KOH at room temperature.

[DOI: 10.1149/1945-7111/ae215e]

Manuscript submitted July 29, 2025; revised manuscript received October 26, 2025. Published December 19, 2025.

Supplementary material for this article is available online

Intensive research has been conducted in the past decades on energy storage and conversion systems, such as water electrolysis to green hydrogen, and on the electrification of the chemical industry to reduce $CO_2$ emissions.[1,2] For efficient electrochemical energy conversions, these processes generally require electrocatalysts with high and stable electrocatalytic activity.[3–5] For many decades, the rotating disk electrode (RDE) has been one of the standard investigation tools for electrocatalytic activity. Its major advantage is the highly controllable and homogeneous mass transport over the electrode. This results in a uniformly accessible electrode, at which the reactant flux is the same at any point on the electrode. This is not only essential for controlled and homogenous mass transport of reactants and products, but also of other additives and impurities, which might influence the reaction. A uniformly accessible electrode is, however, most crucial when studying reactions, which become mass-transport-limited with increasing overpotential. In the case of a mass-transport-limited reaction, the defined mass transport and the uniform accessibility of the RDE allow experimental determination as well as analytical estimation of the reaction kinetics in the mixed-kinetic-mass-transport-dominated regime.[4,6] For this, the Koutecký-Levich (KL) equation can be applied:[7]

$$\frac{1}{I} = \frac{1}{I_{\text{kin}}} + \frac{1}{I_{\text{lim}}} \qquad [1]$$

with the overall current $I$ (A), kinetic current $I_{\text{kin}}$, and mass-transport-limited current $I_{\text{lim}}$.

Apart from the controllable and uniform mass transport and the precise determination of the reduction-oxidation (redox) reaction kinetics, the RDE shows certain disadvantages. Besides the complex and error-prone sample and cell preparation and the incompatibility with industrially relevant conditions, a major drawback is its batch nature, which prevents integration with downstream online analysis.[4,6,8]

Online downstream analysis of the electrolyte becomes essential when studying the electrode stability as it allows the monitoring of electrode dissolution. Thus, coupling electrochemical flow cells (EFCs) with online downstream analysis of the electrolyte has been established as a tool in electrocatalysis to study simultaneously electrocatalytic activity and stability.[3,5,6,9] However, analyzing the reaction kinetics in EFCs according to the KL relation is more difficult because of the complex mass transport. Levich identified that plotting the limiting current against the fluid flow velocity in the center of the channel $u_0$, for different fluid velocities results in a linear correlation, from which, e.g., the diffusion coefficient of the reactive species can be determined. As a simplification when describing the mass transport in EFCs analytically, the axial diffusion is often neglected. When considering the axial mass transport of the reactive species, a boundary layer forms, indicating a decreased reactant concentration at the electrode surface compared to the electrolyte bulk owing to axial mass transport. Due to the characteristic concentration gradient, this boundary layer will be referred to as the diffusion layer in the following. Imaging a small volume unit of reactants, the reactant concentration in this volume unit will deplete because of the consumption by the electrochemical reaction at the electrode while being transported along the electrode by convection. Thus, the boundary layer progressively grows along the electrode, approaching saturation. According to Fick's law, the species flux is inversely proportional to the diffusion layer thickness. As a consequence, the corresponding limiting current density decreases first rapidly and then more slowly over the length of the electrode.[10]

Even though an EFC does not feature a uniformly accessible electrode, Watanabe's group was the first to use the KL equation to study reaction kinetics therein.[11] In 2007, Engelhardt et al. also applied the KL equation to a tubular EFC with the working electrode (WE) mounted on the inner radius of the flow channel. They showed that the relation between the average current density and the limiting current precisely aligns with the KL relation for a one-step reaction of arbitrary order. This correlation was stated to be independent of the electrode length.[12] Later, Scherson et al. validated theoretically that the KL relation can be used with high precision for channel electrodes under certain conditions. They assumed a first-order heterogeneous

---

[=] Equal Contribution.

[z] E-mail: christian.marcks@avt.rwth-aachen.de; anna.mechler@avt.rwth-aachen.de

electron transfer, fixed cell geometry, electrolyte composition, and temperature. Under these conditions, the KL relation was demonstrated to be highly accurate, provided that the ratio of the first-order reaction rate constant $k$ to the central fluid velocity $u_0$ is low (i.e. very small values of $k/u_0^{1/3}$). This corresponds to a slow redox reaction and a fast electrolyte flow. In Scherson's study, the precision of the KL relationship was defined as the slope of the KL plot ($1/I$ *vs* $1/I_{\mathrm{lim}}$), which equals one for uniformly accessible electrodes (see Eq. 1). They suggested the introduction of a multiplication factor of 0.93 (=7% deviation from one) for channel electrodes with very small values of $k/u_0^{1/3}$. For higher values of $k/u_0^{1/3}$, the deviation from one is anticipated to rise. Such a higher ratio of $k/u_0^{1/3}$ due to, e.g., a larger reaction rate indicates that the diffusion limitation sets in earlier compared to smaller values of $k/u_0^{1/3}$.[13]

As a different approach for combining the advantages of continuous flow and uniform accessibility of the electrode, other groups designed flow cells with a nearly uniform limiting current across the electrode. Examples are the wall-jet flow cell,[14] the flow-type scanning droplet cell microscope,[15] the scanning flow cell (SFC),[4] and a specialized V-shaped EFC.[5] Overall, these analytical EFCs feature very small electrodes (0.08–0.5 $\mathrm{cm}^2$) and cell-specific electrolyte flow and positioning of the counter electrode (CE), which is typically not parallel to the WE.[4,15] These characteristics are in contrast to industrial electrolyzers for prominent electrosyntheses like the Chlor-Alkali[16] and water electrolysis.[17] Such electrolyzers consist of planar, parallel electrodes of much larger scale (0.1–5 $\mathrm{m}^2$) with a separator between the anode and cathode chamber, and an electrolyte flow parallel to the electrode. The differences in electrolyte flow and cell geometry between the analytical EFCs and industrial electrolyzers can result in different mass transport to the electrode and dead zones. Thus, gas removal and accumulations of products, starting materials, or other additives might vary. This can not only influence the product distribution, but also the electrode performance and stability. The cell-specific arrangement of CE and WE within analytical EFCs introduces an inhomogeneous current distribution at the WE, which could induce inhomogeneous catalyst use and degradation. It becomes even more challenging when scaling up the electrodes. The larger the electrodes, the more pressure gradients, bubble curtains, inhomogeneous flow velocity distributions (jets, dead zones), or an increasing diffusion layer thickness along the electrode length become important.[10] This shows that the knowledge transfer from these analytical EFCs to an industrial scale is difficult. Hence, to facilitate it, more advanced concepts need to be developed.

To sum up, the flow cells that can be both analytically described and used with online downstream analysis are not representative of industrial conditions. On the other hand, attempts have been made to analytically describe the mass transport in different EFCs but these EFCs were not combined with online downstream analysis.

In this work, we report an EFC with a WE area of 1 $\mathrm{cm}^2$ for coupling with downstream online analysis, such as inductively coupled plasma optical emission spectroscopy (ICP-OES), and simultaneous activity determination of the electrocatalyst. Such an EFC will be herein referred to as online-coupled EFC. To evaluate the design, we use COMSOL Multiphysics to model fluid flow velocity, concentration distribution, and particle flux of the reactive species over the electrode surface. First, simply scaled-up versions of reported online-coupled EFCs, namely the SFC from Mayrhofer et al.[4] and the V-shaped EFC (V-EFC) from Schlögl et al.[5] with an electrode area of 1 $\mathrm{cm}^2$, are simulated and compared. On this basis, we establish criteria for designing an online-coupled EFC with 1 $\mathrm{cm}^2$ parallel electrodes (pEFC), ensuring a precise activity determination over a wide potential range and minimal dilution of reaction products. To investigate the influence of mass transport of the reactive species to the electrode on the precision of the activity determination, uniform accessibility and uniformity of convective mass transport over the WE are varied. The precision is quantified by the deviation of the KL slope from one and the so-called $G$ value, which describes the deviation of the simulated kinetic current density, obtained from the KL plot, from the kinetic current density, calculated with the input parameter according to Butler-Volmer. The prototype of the final design is 3D-printed. The simulations and applicability of the kinetic analysis for electrocatalysts are experimentally verified for the ferricyanide reduction as an electrochemical model reaction. Based on this designed pEFC, it is explored how the potential can be precisely controlled and determined for the oxygen evolution reaction (OER) during constant current operation at industrially more relevant conditions, i.e. up to 30 wt% KOH, 80 °C and 100 mA $\mathrm{cm}^{-2}$. Lastly, online monitoring of the Fe concentration during cyclic voltammetry (CV) and chronopotentiometry (CP) at 10 mA $\mathrm{cm}^{-2}$ is demonstrated with a Ni-Fe WE in 1 M KOH at room temperature. With the pEFC developed in this work, the activity and stability of novel catalysts can now be evaluated under conditions closer to industrial application, facilitated by using parallel 1 $\mathrm{cm}^2$ electrodes and a uniform parallel flow distribution.

## Experimental

***Numerical simulations.***—In order to design the pEFC, the distribution of fluid flow velocity, reactant concentration, and species flux were simulated with COMSOL Multiphysics for different cell geometries.

The approach for modeling the fluid flow velocity, reactant concentration, and species flux at the electrode in an EFC is based on previous works on the KL analysis for the oxygen reduction reaction in the SFC.[6] All relevant model parameters are summarized in Table S-1 in the Supporting Information.

The simulation modeled a laminar aqueous flow, which was coupled to the transport of diluted species. The electrolyte flow was modeled by incompressible ($\nabla \boldsymbol{u} = 0$) Navier–Stokes equations and solved for fluid flow velocity and pressure:

$$\rho \frac{\partial \boldsymbol{u}}{\partial t} + \rho(\boldsymbol{u}\cdot\nabla)\boldsymbol{u} = \nabla[-p\boldsymbol{I} + \mu_{\mathrm{dyn}}(\nabla\boldsymbol{u} + (\nabla\boldsymbol{u})^{\mathrm{T}})] + \boldsymbol{F}. \qquad [2]$$

with the density of the fluid $\rho$ (kg $\mathrm{m}^{-3}$), the flow velocity field $\boldsymbol{u}$(m $\mathrm{s}^{-1}$), the time $t$ (s), the Nabla Operator $\nabla$, the pressure $p$ (Pa), the unity matrix $\boldsymbol{I}$, the dynamic fluid viscosity $\mu_{\mathrm{dyn}}$ (Pa s), and a volume force on the system $\boldsymbol{F}$(N).

External force on the system ($\boldsymbol{F} = 0$) was neglected and a stationary state ($\partial \boldsymbol{u}/\partial t = 0$) assumed.

The concentration field of reactive species was calculated by the Nernst-Planck equation (Eq. 3), neglecting the migration of ions in the electrical field as a high ionic conductivity was assumed:

$$\nabla\cdot(-D\,\nabla c) + \boldsymbol{u}\cdot\nabla c = \frac{\partial c}{\partial t} + K. \qquad [3]$$

with the diffusion coefficient $D$ ($\mathrm{m}^2\ \mathrm{s}^{-1}$), the concentration $c$ (mol $\mathrm{m}^{-3}$), and the volumetric homogeneous reaction rate $K$ (mol $\mathrm{m}^{-3}\ \mathrm{s}^{-1}$).

To solve Eq. 3, a steady-state regime ($\partial c/\partial t = 0$) and the absence of homogeneous reactions ($K = 0$) is assumed.

Furthermore, the following boundary conditions were introduced: For the hydrodynamic flow equations, the flow velocity at the fluid-wall interface was set to zero (no-slip condition). The laminar flow boundary condition was defined as an average flow velocity at the inlet and atmospheric pressure at the outlet. For the species transport equations, no flux was assumed at the walls including in- and outlet. A constant inflow concentration of active species $c_{\mathrm{inlet}}$ was defined as an inlet boundary condition, while the backflow of the species at the outlet was suppressed. At the electrode surface, the flux of reactive species was modeled according to a first order, Butler-Volmer-like reaction kinetic (Eq. 4).[6]

$$J_{\mathrm{BV}} = -\frac{i_0 c}{Fzc_{\mathrm{inlet}}} \exp\left(-\frac{\alpha F}{RT}\eta\right) \qquad [4]$$

with the species flux $J$ (mol $\mathrm{m}^2\ \mathrm{s}^{-1}$), exchange current density $i_0$ (A $\mathrm{m}^2$), Faraday constant $F$ (As $\mathrm{mol}^{-1}$), the number of exchanged electrons $z$ (-), charge transfer coefficient $\alpha$ (-), universal gas constant $R$ (C $\mathrm{mol}^{-1}$), temperature $T$ (K), and overpotential $\eta$ (V). As per convention, a negative current is set since the simulated reaction is a reduction reaction of first order. Normalizing the concentration is necessary to account for mass transport effects at large overpotentials.

The kinetic and electrolyte parameters were set comparable to those found in the oxygen reduction reaction, resembling a simple, irreversible, and slow first order electrochemical reaction.

All simulations were performed using finite element software COMSOL Multiphysics 5.6. with the model geometry constructed in Autodesk Inventor 2021. For details regarding the simulation model and the meshing incl. the mesh independence study, please see the Supporting Information (Fig. S-1).

The model was solved for the velocity field $\boldsymbol{u}$, the concentration $c$, and pressure $p$ using the default steady-state solver for flow and concentration and a segregated solution sequence. The flow rate at the inlet was varied in the simulation between 0.03 mL min$^{-1}$ and 9.18 mL min$^{-1}$ for the flow geometry of the SFC, V-EFC, and the final herein-designed pEFC. For the simulation of the pEFC's preliminary flow geometry with a reduced cell width of 0.25 cm (see Fig. 4), the volume flow was varied between 0.007 mL min$^{-1}$ and 1.829 mL min$^{-1}$. Please note that the model geometry was divided in half by a symmetry plane and only half of the model geometry was simulated to save calculation time and capacities. The specified flow rates are, hence, defined for half of the inlet's cross-section. The overpotential was swept from 0.3 V to 1.5 V in 0.05 V potential steps, and ohmic losses were not considered in the simulation. To evaluate the Levich analysis and the KL relation for the different EFC designs, the resulting average flux at the electrode was translated into the respective current by multiplication with $z$ and $F$.

Flow velocity, concentration, and species flux distribution were analyzed qualitatively. For the Levich analysis, $i_{\mathrm{lim}}$ was plotted against $u_0^{1/3}$ to verify the linear relation. Here, it needs to be noted that while the simulated limiting currents all follow the expected Levich relation ($I_{\mathrm{lim}} \propto u_0^{1/3}$), their absolute values deviate from the analytical solutions, which can be calculated with the equations from Scherson et al.,[13] Compton et al.[18] and O'Neil et al.[19] This discrepancy likely arises from simplifications in the numerical model and residual mesh dependency, leading to an overestimation of mass transport. However, since the expected proportionality ($I_{\mathrm{lim}} \propto u_0^{1/3}$) was reproduced, the main conclusions regarding the mass-transport behavior remain valid. Quantitatively, the deviation of the simulated kinetic current density $i_{\mathrm{kin,sim}}$, obtained from the KL plot, from the kinetic current density $i_{\mathrm{kin,input}}$, calculated with the input parameter according to Butler-Volmer, was investigated. This deviation served as evaluation parameter $G$ for the homogeneity of the mass transport and, thus, $i_{\mathrm{lim}}$ over the electrode, and it is defined as:

$$G = \frac{i_{\mathrm{kin,sim}} - i_{\mathrm{kin,input}}}{i_{\mathrm{kin,input}}} \cdot 100 \qquad [5]$$

Exemplary polarization curves and KL plots can be seen in Fig. S-2. $I_{\mathrm{kin,sim}}$ can be read as the inverse of the $y$-axis intercept of the fitted KL plot and converted into the respective current density $i_{\mathrm{kin,sim}}$.

***The designed pEFC.***—In this work, the pEFC with 1 cm$^2$ parallel electrodes for online downstream analysis of the electrolyte was designed. It was used to validate the simulations of the pEFC (Fig. 1a) and to investigate simultaneously the activity and stability of electrocatalysts for the alkaline water electrolysis (AWE). To investigate the AWE electrocatalysts, the pEFC in Fig. 1a was adjusted, and its design can be seen in Fig. 1b.

The pEFC represents two interconnected rectangular channels, each with an angle of (a) 60° and (b) 30° to the bottom. Toward the in- and outlet, the rectangular-shaped channels change into a round tube with a diameter of 2 mm. The CE and WE are situated in the middle section between the in- and outlet with (a) 1 mm and (b) 3 mm distance. This results in (a) a 10 × 1 mm and (b) a 10 × 3 mm channel cross-section over the WE. For design A (Fig. 1a), the CE (1 × 1 × 0.1 cm, SIGRADUR G Glassy Carbon, HTW) is seamlessly inserted by adhesive into the 3D-printed top part of the flow cell and electrically contacted by a brass rod (diameter $d$ = 4 mm) and Ag-containing conductive adhesive (8330S, MG Chemicals). For design B (Fig. 1b), an exchangeable CE is used. The exchangeable CE refers to a 1 × 1 × 0.1 cm glassy carbon plate, which is contacted by a brass rod ($d$ = 4 mm) and conductive adhesive, and is embedded (EpoHeat CLR, Buehler) in a 3D-printed (AR-M2, rapidobjects) holding structure. The WE is embedded (CaldoFix-2 for 1 M KOH, RT and EpoHeat CLR for 30 wt% KOH, 80 °C) as well into a 3D-printed form (Veroclear, a: 20 × 25 × 10 mm, b: 20 × 30 × 10 mm) to define its dimensions and position. A reference electrode (RE) with a 6 mm diameter can be placed in a reservoir, which is connected to the inlet channel by a capillary with a diameter of 1 mm. It needs to be considered that if the electrode-contact configuration for the WE or CE is changed, this likely influences the resistance of the system and, thus, static as well as dynamic electrochemical measurements.

Prototypes of the pEFCs were 3D-printed by the Objet Eden260V-Stratasys printer with a resolution of 20 μm.[20] VeroClear (Stratasys) was used as material with material properties similar to polymethyl methacrylate. For 30 wt% KOH and 80 °C, the top-part of the pEFC, the CE-holder, and the CE-screw were 3D-printed in AR-H1 or AR-M2. Due to the performed material tempering for AR-H1, the threads must be recut after printing.

***Experimental validation of the Levich and KL equation.***—To experimentally validate the applicability of the Levich analysis and the KL equation for the pEFC designed herein and shown in Fig. 1a, the kinetics of the ferricyanide reduction were investigated at different flow rates.

Before the electrochemical experiment, the embedded WE (1 × 1 cm, glassy carbon) was polished with an alumina-water-slurry (MicroPolish Suspensions, MicroCloth Polishing pads, Buehler) with decreasing grain size (1 μm, 0.3 μm, 0.05 μm), ultrasonicated in ultrapure water (Type 1, 0.05 μS cm$^{-1}$) for 5 min, and dried. A Hg/HgSO$_4$ RE (RE-2CP, ALS) and 10 mM $K_3[Fe(CN)_6]$ (<10 μm, 99%, Sigma-Aldrich) in 0.1 M $HClO_4$ as electrolyte were used. The electrolyte was prepared from ultrapure water (Type 1, 0.05 μS cm$^{-1}$) and 70% $HClO_4$ (Supra, Carl Roth). From the Ar-purged reservoir with a volume of 200 mL, the electrolyte ran through the flow cell and into an electrolyte waste at different flow rates (0.5, 1, 1.2, 1.3, 1.4, 1.5, 2 mL min$^{-1}$, 4 channels à 12 rolls, Ismatec Reglo Digital Pump, Masterflex). The electrolyte volume in the reservoir was kept constant over the course of the experiment by redosing with the same flow rate. For each flow rate, the electrolyte resistance was determined by electrochemical impedance spectroscopy (EIS) (10 Hz—300 kHz, 10 mV$_{\mathrm{rms}}$) at open circuit potential (OCP), and three linear sweep voltammograms (LSVs) from 0.79 to –0.01 V *vs* RHE at 2 mV s$^{-1}$ were performed with an Interface 1010E potentiostat (Gamry Instruments). Potentials are reported 100% $iR_u$ corrected and *vs* RHE (see Supporting Information for conversion into RHE-scale).

***Electrochemical impedance spectroscopy measurements for the investigation of the electrode positioning.***—To investigate the applicability of EIS depending on the relative electrode positioning in different pEFC designs, EIS measurements were performed in 1 M KOH with a Ni WE (99.0%, Goodfellow). First, the Ni plate WE was ground (7000 grit, STARCKE), sonicated in ethanol and ultrapure water for five minutes each, and assembled into the EFC. Electrical contact was established by self-adhesive Cu tape (Conrad). A glassy carbon CE as rod ($d$ = 1 mm) or 1 × 1 cm plate, a Hg/HgO RE (RE-61AP, ALS), and a flow rate of 1 mL min$^{-1}$ (Ismatec Reglo Digital Pump, 4 channels à 12 rolls) were applied. The WE was conditioned by CV (1–1.45 V *vs* RHE, 10 mV s$^{-1}$, 50 cycles). Following, EIS was performed between 300 kHz and 10 Hz at OCP with an amplitude of 10 mV$_{\mathrm{rms}}$ and 10 points per decade.

***Online electrolyte monitoring while studying alkaline oxygen evolution electrocatalysts.***—To study the electrolyte composition online during an electrochemical experiment, the AWE-pEFC

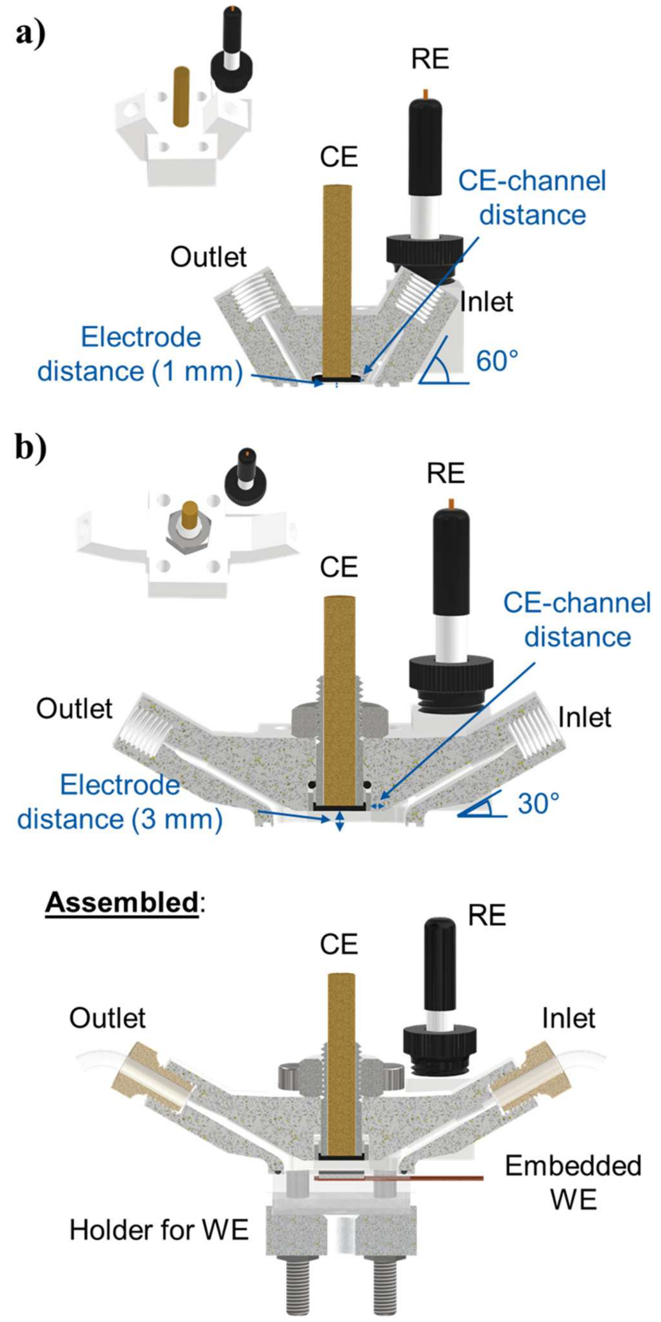

**Figure 1.** Final design of the (a) orginal pEFC and (b) AWE-pEFC with 1 $cm^2$ WE and CE. The RE is connected to the inlet channel by a capillary. The cell features a channel diameter of 2 mm, a reaction volume of (a) 10 × 10 × 1 mm and (b) 10 × 10 × 3 mm, and an angle of (a) 60° and (b) 30° between the channels and the bottom. WEs are embedded into form and are placed at the bottom. The differences between designs A and B are indicated in blue.

(Fig. 1b) was connected to the ICP-OES. Online ICP-OES was performed with an Agilent 5800 VDV ICP-OES system to determine the metal concentrations in the electrolyte with the operating parameters listed in Table I. A concentric standard SeaSpray nebulizer, standard quartz torch, and humified Ar were applied. Online ICP-OES was performed with the so-called time scan option. Here, data is continuously recorded without the shutter of the detector being closed. The time resolution corresponds to the measuring time of a single data point since no repeats are done. The minimum measuring time is limited to 3 s.

**Table I. Operating parameters for the ICP-OES.**

| Parameter | Value |
|---|---|
| Measuring time/s | 3 |
| HF-Power/kW | 1.2 |
| Stabilizing time/s | 0 |
| View | Axial |
| Nebulizer gas flow/l $min^{-1}$ | 0.65 |
| Plasma gas flow/l $min^{-1}$ | 12 |
| Auxiliary gas flow/l $min^{-1}$ | 1 |
| Background correction | Automatic |
| Pump rate/U $min^{-1}$ | 10 (white-white) |

Online ICP-OES of the electrolyte coupled to the pEFC was applied to investigate the behavior of Ni-Fe alloy electrodes with 30 wt% of Fe ($Ni_{70}Fe_{30}$) as anodes in 1 M KOH for the alkaline water electrolysis. The WE preparation, RE choice, and cell assembly were employed according to the procedure described in our previous work.[21] The $Ni_{70}Fe_{30}$ WE (HMW Hauner) was ground (7000 grit size, STARCKE), polished with an alumina-water-slurry (MicroPolish Suspensions, MicroCloth Polishing pads, Buehler) with decreasing grain size (1 μm, 0.3 μm, 0.05 μm), ultrasonicated in ultrapure water (Type 1, 0.05 μS $cm^{-1}$) for 5 min, and dried. Experiments were conducted at ambient pressure and room temperature (20 °C–25 °C). 1 M KOH was prepared from KOH pellets (min. 85% KOH, CHEMSOLUTE) and ultrapure water. The Fe concentration was adjusted to 110 ± 10 ppb by adding Fe in diluted $HNO_3$ in the form of an ICP-OES calibration standard (ICP-026, Agilent Technologies). The electrolyte ran through the vertically aligned flow cell into the ICP-OES with 1 mL $min^{-1}$ from the Ar-purged PTFE reservoir. The Fe concentration was determined by measuring at 238.204 nm. K (404.414 nm) was measured as the internal standard, and Ar (420.067 nm) as a temperature sensor. Calibration (3 points between 10–500 ppb [*e.g.* 10, 100, 500 ppb] + blank, in 1 M KOH, 5 min per calibration point) was performed separately, and ICP-OES was run with ultrapure water between the calibration points. The resulting signal was averaged over 3 min. Before starting the electrochemical protocol, a baseline of at least 5 min was recorded. The electrochemical protocol consisted of EIS at OCP (100 kHz-10 Hz, 10 $mV_{rms}$), followed by three CVs (–0.35–1.6 V *vs* RHE, 2 mV $s^{-1}$) and a CP at 10 mA $cm^{-2}$ for 30 min. Data evaluation was done with a custom Python script, as in our previous work.[21,22] Spectra were smoothed with a moving average over 3 data points. In case of intense gas evolution, the outlying data points were omitted, with no trends modified.

In order to elucidate the peak smearing behavior when coupling the ICP-OES with the herein-designed pEFC, a Ni dissolution experiment was conducted with a $Ni_{99.99}$ WE (99.99+ wt.% Ni, HMW Hauner), a 1 × 1 cm glassy carbon CE, and a $Hg/HgSO_4$ RE in 0.1 M $HClO_4$. The experimental procedure was conducted as described under *Experimental Validation of the Levich and KL equation.* Before the experiment, the CE was additionally ground (2500, 5000 grit size), ultrasonicated in ultrapure water for 5 min, and dried. The calibration was performed with 0.1 M $HClO_4$ as solvent. The Ni concentration was determined by measuring at 231.604 nm. The Ar line (420.067 nm) was detected as a temperature sensor of the plasma. As an electrochemical protocol, an OCP was applied first, followed by CV conditioning (0.056–1.256 V *vs* RHE, 200 mV $s^{-1}$, 30 cycles), a 15 min pause, and 10× a CP at 1 mA $cm^{-2}$ for 10 s with a 10 min OCP between each potential step.

For the analysis of AWE electrocatalysts as well as the Ni dissolution, the potentials were 100% $iR_u$ corrected and reported *vs* RHE (see Supporting Information for conversion into RHE-scale). The electrolyte resistance was determined at OCP for the value where the phase shift was closest to zero.

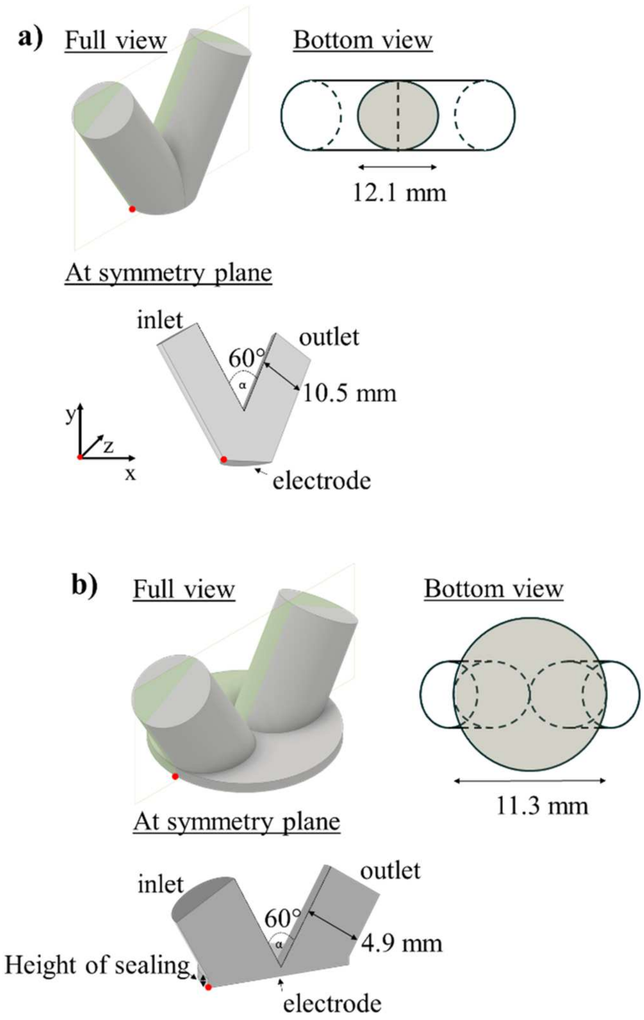

**Figure 2.** Scheme of flow geometries utilized for the numerical simulations of a) the SFC and b) the V-EFC, with a) $\alpha = 60°$, $d = 10.5$ mm, 1 cm$^2$ electrode and b) $\alpha = 60°$, $d = 4.9$ mm, 1 cm$^2$ electrode, sealing height of 0.64 mm.

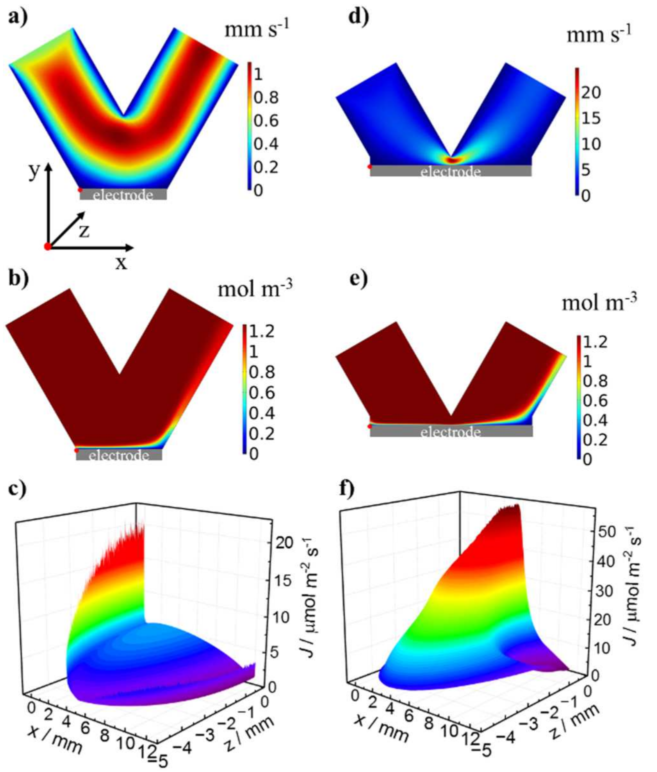

**Figure 3.** Flow velocity distribution (a, d) and concentration distribution (b, e) at the central x-y plane of the cell (symmetry plane) and species flux at the electrode (c, f) for the SFC (a-c) and the V-EFC (d-f). The average inlet volume flow is 1.45 mL min$^{-1}$ (for half of the inlet's cross-section), and the overpotential is 1.5 V. The scale ranges from 0–1.1 mm s$^{-1}$ (a), 0–24.7 mm s$^{-1}$ (d), and 0–1.26 mol m$^{-3}$ (b, e).

## Results and Discussion

***Simulation of the scale-up of the reported SFC*** [4,6] ***and V-EFC***[5]**.—**In order to find a suitable online-coupled EFC for 1 cm$^2$ electrodes, we investigated the reported flow cells for coupling with ICP-OES for scale-up. The flow geometry of the SFC from Mayrhofer et al.[4] and the V-EFC from Schlögl et al.[5] can be seen in Fig. 2. The SFC cell design consists of two intersecting channels in a V-geometry with 60° between the channels and the bottom, forming an elliptical opening at the bottom of the cell. The CE is placed into one of the channels and the RE is connected to the respective other channel by a capillary or T-connector.[3,4,6] In contrast to the SFC, the flow channels of the V-EFC intersect at their outer walls and it features a circular opening, resulting from an O-ring-sealing. The RE and CE are placed in the channels.[5] For the scale-up, the electrode area was fixed to 1 cm$^2$.

The simulation results for the flow velocity distribution, concentration distribution, and species flux in a mass-transport-limited case can be seen in Fig. 3 for a volume flow of 1.45 mL min$^{-1}$ at the inlet and an overpotential of 1.5 V. Please note that, here and in the following, the volume flow is defined for the inlet's cross-section of the simulated cell width, which is half of the entire cell due to the symmetry plane. Thus, the flow rate is given for half of the inlet's cross-section. The flow velocity (a, d) and concentration (b, e) distribution are shown at the central x-y plane of the cell (z=0), corresponding to the symmetry plane in the middle of the channel. The species flux (c, f) at the electrode is shown in the x-z plane (y=0) from the channel wall to the symmetry plane.

In Fig. 3a, the flow velocity distribution for the SFC shows a maximum velocity of 1.1 mm s$^{-1}$ in the middle of the channel and no turbulence, such as a vortex. Note that due to the V-shaped channels, the flow velocity distribution is not uniform over the WE. The highest velocity can be found at the intersection of the channels, while there are regions with lower flow velocity toward the outer channel walls (x = 0 and x = 12). The corresponding concentration (Fig. 3b) is non-uniformly distributed over the WE. At the electrode, the concentration of active species is zero because of its consumption. Along the electrode with increasing x, the reaction species is continuously consumed, the concentration gradient decreases, and the diffusion layer grows as diffusion is too slow for equilibration. At the symmetry plane (z = 0, central x-y plane), the diffusion layer thickness varies from approx. 1 mm at the inlet (x ≈ 0) to 3 mm at the outlet (x ≈ 12). Figure 3c shows the species flux at the electrode and demonstrates more clearly how this non-uniformity evolves along the electrode in the x-direction. The maximum species flux of 22 μmol m$^{-2}$ s$^{-1}$ occurs at the start of the electrode (x ≈ 0) and rapidly drops to approx. 5 μmol m$^{-2}$ s$^{-1}$ after less than 1 μm along the electrode. Until approx. 3 mm (x ≈ 3), the species flux stays relatively constant with a slight increase in the species flux resulting from the increase in flow velocity over the WE toward the center of the electrode. After that, the species flux continues to decrease to a minimum of 0.9 μmol m$^{-2}$ s$^{-1}$. The increase in species flux at the end of the electrode appears unphysical as here the flow velocity is zero and the species flux should be similarly low. Thus, this is considered an artifact. While only a few data points deviate, the surface plot exaggerates the effect due to interpolation between points. Along the *z*-axis, the species flux decreases toward the cell walls (z = –5). The average species flux over the WE is 3.8 μmol m$^{-2}$ s$^{-1}$.

Qualitatively, these results reflect the previous simulations for the smaller SFC version.[6] Though, the absolute maximum velocity and, thus, $i_{\text{lim}}$ is about 17× lower for the scaled-up version despite the larger inlet volume flow of 1.45 mL min$^{-1}$ compared to 1 mL min$^{-1}$ for the smaller SFC. This indicates a smaller kinetic regime, in which the material properties can be analyzed. The KL evaluation identifies a KL slope of 1.0, which indicates a more homogeneous $i_{\text{lim}}$ over the electrode area and, thus, a better applicability of the KL analysis compared to the reported deviation of about 6% in the case of the small cell model.[6] However, the discrepancy between the small cell model and the one simulated here is more likely due to slight differences in the simulation, *e.g.* the meshing. Downstream online analysis such as ICP-OES, however, restricts the maximum volume flow to avoid non-spectral interferences. If excessive amounts of sample are introduced into the plasma, the plasma is destabilized, which can cause poor reproducibility. Such a low volume flow would result in an earlier onset of the mass transport limitation. The resulting small kinetic regime of the scaled-up SFC would, therefore, highly limit its applicability for the analysis of the catalyst's kinetics.

For the V-EFC, the flow velocity distribution in Fig. 3d shows a laminar flow in the channels with a maximum of 4.5 mm s$^{-1}$ in the middle of the channel. When meeting the electrode, the flow accelerates at the intersection of the channels to a maximum of 25 mm s$^{-1}$. The flow velocity decreases toward the cell walls ($x = 0$, $x = 11$, $z = –5$, and $z = 5$). The resulting concentration distribution (Fig. 3e) is non-uniform and asymmetrical. The smallest diffusion layer thickness of 0.14 mm is allocated at the highest flow velocity over the WE; the largest diffusion layer thickness of 2.3 mm is obtained at the outlet ($x \approx 11$). The corresponding species flux (Fig. 3f) shows a maximum of 56 μmol m$^{-2}$ s$^{-1}$ in the center of the electrode, where also the highest flow velocity over the WE and smallest diffusion layer thickness is located. The centrally allocated and high species flux decreases in all directions. Along the *x*-axis, it decreases slowly toward the beginning of the electrode ($x = 0$) and more rapidly toward the end of the electrode ($x = 11$). The asymmetrical distribution of species flux and concentration might result from a trade-off between high flow velocity, which is very localized in the center over the electrode, and axial diffusion along the electrode in the direction of the flow. The average species flux over the electrode is 19 μmol m$^{-2}$ s$^{-1}$, being significantly higher than that one of the scaled-up SFC, indicating a larger kinetic regime. The KL evaluation identifies a small deviation of the KL slope of 1% from 1. To evaluate the geometries further, a more sensitive measure is required, and for that, the *G* value is taken in the following. The *G* value is another measure for the homogeneity of the mass transport, expressed by the deviation of the simulated kinetic current density $i_{\text{kin,sim}}$, obtained from the KL plot, from the kinetic current density $i_{\text{kin,input}}$, calculated with the input parameter according to Butler-Volmer (see *Numerical Simulations* under *Experimental*). For the scaled-up SFC, the *G* value equals 5%, and for the V-EFC, *G* is 7%, which is still comparable to the SFC. Thus, the scaled-up V-EFC features a sufficiently large kinetic regime and precise activity determination. Regardless, it must be considered that this high precision results from the $i_{\text{lim}}$ being scattered around the median and does not refer to a homogeneous species flux over the electrode area. The identified regions of this design with an extremely low flow velocity and species flux (i.e., dead zones) should not be neglected. Depending on the application, these points can be a challenge, e.g., if the aimed product is converted further at the electrode, affecting the product distribution, or inhomogeneous catalyst usage and degradation can occur. Such inhomogeneous catalyst usage might falsify the catalyst performance data. Additionally, the current distribution at the WE could become difficult with a rod-shaped cathode in only one channel. Since the tip of the CE rod would be the closest to the WE, the potential drop due to the electrolyte resistance would be the smallest there. Thus, the circular area of the rod would need to be increased to approx. 1 cm$^2$, which would again increase the channel and the WE. Similar considerations for the herein-designed pEFC are discussed later. Lastly, the discrepancy between the V-EFC and the cell designs in the industry and classical lab-scale testing needs to be considered.

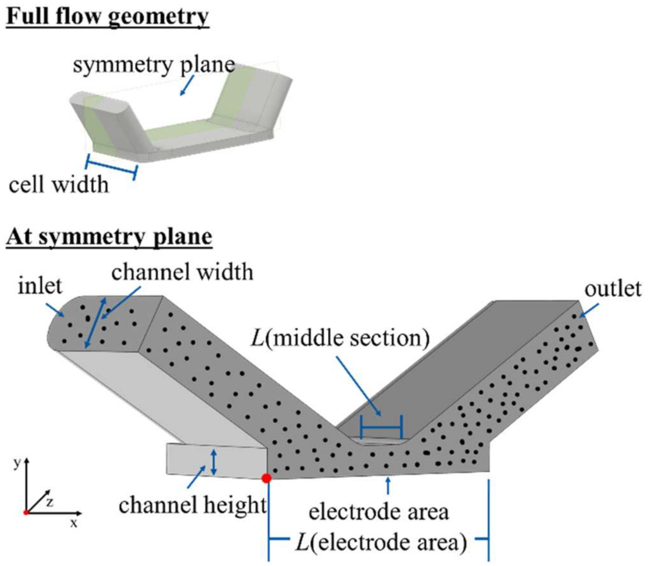

**Figure 4.** Schematic flow geometry, utilized for the numerical simulations to design the pEFC. Simulations were performed with 1 mm channel height, varying channel widths of the in- and outlet, varying electrode lengths, and 2.5 mm cell width (symmetry plane at 1.25 mm).

***Criteria for the scale-up of an online-coupled EFC.***—Based on the modeled scale-up of the reported flow cells, we designed a first flow geometry for the pEFC as seen in Fig. 4. Here, the possibility of kinetic analysis and compatibility with downstream analysis was included. Online downstream analysis, such as ICP-OES, restricts the maximum electrolyte flow to avoid non-spectral interferences and the dilution of the electrochemical products. For kinetic analysis, a large kinetic regime and uniform mass transport over the WE are important to apply the KL analysis. Consequently, a minimal reaction volume over the electrode is required for high convection and minimal dilution of reaction products. This design also encompasses planar, parallel electrodes with electrolyte flow parallel to the electrode as industrial characteristics. As a result, cross-contaminations from CE reactions cannot be excluded. These considerations entail two interconnected rectangular channels, tilted in a V-shape (Fig. 4). This channel geometry allows the minimal reaction volume over the WE and fewer dead zones.

To adjust this design for the applicability of the KL analysis, the mass transport of reactive species to the electrode was characterized. Here, two effects were looked at separately: the flow velocity distribution over the WE due to convection and the electrode's accessibility with a uniform flow velocity distribution over the WE. For the simulations, a geometry model with a reduced cell width was used to minimize calculation time, assuming the cell width does not influence the model (width ($z$) $= 0.25$ cm, length ($x$) $= 1–4$ cm, $A = 0.25–1$ cm$^2$, symmetry plane at $z = 0.125$ cm, simulated: $0 < z_{\text{sim}} < 0.125$ cm, $A_{\text{sim}} = 0.125–0.625$ cm$^2$). Thus, please note that the absolute flow velocities, concentrations, and species fluxes are not comparable to the scaled-up SFC and V-EFC (Fig. 3) and the final EFC design presented (Fig. 7).

***Influence of flow velocity distribution over the WE.***—When evaluating the influence of the flow velocity distribution over the WE on the KL analysis, it is known that the more uniform the flow velocity distribution over the WE, the narrower the distribution of $i_{\text{lim}}$ and the better the applicability of the KL analysis.[10] Herein, the extent of imprecision introduced by an inhomogeneous convective mass transport on the kinetic analysis was estimated for different versions of the pEFC's flow geometry, which is presented in Fig. 4.

Therefore, the uniformity of the flow velocity distribution over the WE was varied by changing the channel width (CW) of the in- and outlet, while the WE covered the entire bottom part of the cell. The transition zone between the connecting middle section and the channels introduces inhomogeneity of the flow velocity distribution. Thus, the ratio $U$ between the length of the middle section, $L$(middle section), and the length of the electrode, $L$(electrode), was defined to quantify the share of the electrode with parallel flow:

$$U = \frac{L\,(\text{middle section})}{L\,(\text{electrode})}\cdot 100\% \qquad [6]$$

In Fig. 5, the velocity flow distribution and species flux for CWs of 2 mm (a, b), 1 mm (c, d), and 0.5 mm (e, f) for 1.14 mL $\text{min}^{-1}$ at 1.5 V are displayed, corresponding to the mass-transport-limited case. The respective concentration distributions are shown in Fig. S-3. The smallest CW of 0.5 mm corresponds to the largest $U$ of 73.3%. For a CW of 2 mm, less than a quarter of the electrode (13.3%) features a parallel flow to the electrode.

Figure 5 identifies in (a), (c), and (e) a uniform flow velocity distribution over the electrode in the middle section with a maximum velocity of 27 mm $\text{s}^{-1}$. The species flux distribution at the electrode is shown in Figs. 5b, 5d and 5f. If $U$ is large (CW = 0.5 mm, Fig. 5f), the maximum flux of 83 μmol $\text{m}^{-2}$ $\text{s}^{-1}$ will be closest to the beginning of the electrode at the inlet ($x \approx 1$ mm). When the CW is increased (compare Figs. 5b, 5d), and $U$ becomes smaller, the point of maximum species flux moves toward the center of the electrode. For the largest CW of 2 mm (Fig. 5b), the maximum species flux of 49.4 μmol $\text{m}^{-2}$ $\text{s}^{-1}$ is located at 4 mm along the electrode. As previously discussed, the homogeneity of the species flux over the electrode is directly correlated to the uniformity of the convective and diffusional mass transport. The larger $U$, the more the species flux distribution is dominated by axial diffusion limitation. For smaller $U$, the species flux distribution shows a trade-off between the limitation by convection and axial diffusion. The KL analysis supports this visual correlation. The evaluation parameter $G$ for the homogeneity of the mass transport increases with decreasing $U$ from 0.5% ($U = 73\%$, 0.5 mm CW) to 3% ($U = 53\%$, 1 mm CW) to 8% ($U = 13\%$, 2 mm CW). This evaluation shows that even if only 13% of the electrode features a uniform flow velocity distribution, the imprecision of the $i_{\text{kin}}$ determination *via* the KL analysis is still acceptable. Especially when comparing the KL slopes, which were all ranging between 0.986–0.990, to the reported 0.94 from Kulyk et al.[6] and Scherson et al.[13] Still, to obtain the highest possible precision in the activity determination, the WE should be placed in the connecting middle section with parallel flow to the electrode.

***Influence of uniform accessibility.***—Even though EFCs do not have a uniformly accessible electrode, the KL analysis was previously applied to EFCs.[11–13] This work, indeed, aims to evaluate the significance of uniform accessibility in determining reaction kinetics within laboratory-scale EFCs. For that, the electrode length was increased from 1 to 4 cm with a parallel flow and a uniform flow velocity distribution over the entire electrode, which is ensured by placing it in the middle section.

Figure 6 shows the concentration distribution (a, b) and species flux (c, d) at the central x-y plane for an electrode length of 1 cm (a, c) and 4 cm (b, d) for an inlet volume flow of 1.14 mL $\text{min}^{-1}$ at 1.5 V, corresponding to the mass-transport-limited case. The flow velocity distribution is given in Fig. S-4. For better visualization of the reactive species' depletion along the length of the electrode, the concentration distribution at a lower flow rate (14.4 μL $\text{min}^{-1}$) is shown in Figs. 6a and 6b). For the 1 cm and 4 cm long electrodes, Fig. 6 indicates an increasing diffusion layer thickness along the electrode length in the direction of the flow with a maximum diffusion layer thickness at the end of the electrode. For a flow rate of 1.14 mL $\text{min}^{-1}$, a diffusion layer thickness of 0.4 mm ($L$(electrode) = 1 cm, a) and >1 mm ($L$(electrode) = 4 cm, b) was calculated. Additionally, the species flux in Figs. 6c and 6d) indicates more clearly the diffusion layer thickness along the electrode. For both electrode lengths, the species flux shows a maximum at the very beginning of the electrode. At the central x-y plane, the species flux of approx. 0.5 mmol $\text{m}^{-2}$ $\text{s}^{-1}$ rapidly drops down to 1/10 of its original value after 130 μm, after which it stays comparatively constant along x. Along the $z$-axis, the species flux decreases toward the cell walls. Thus, the depicted concentration

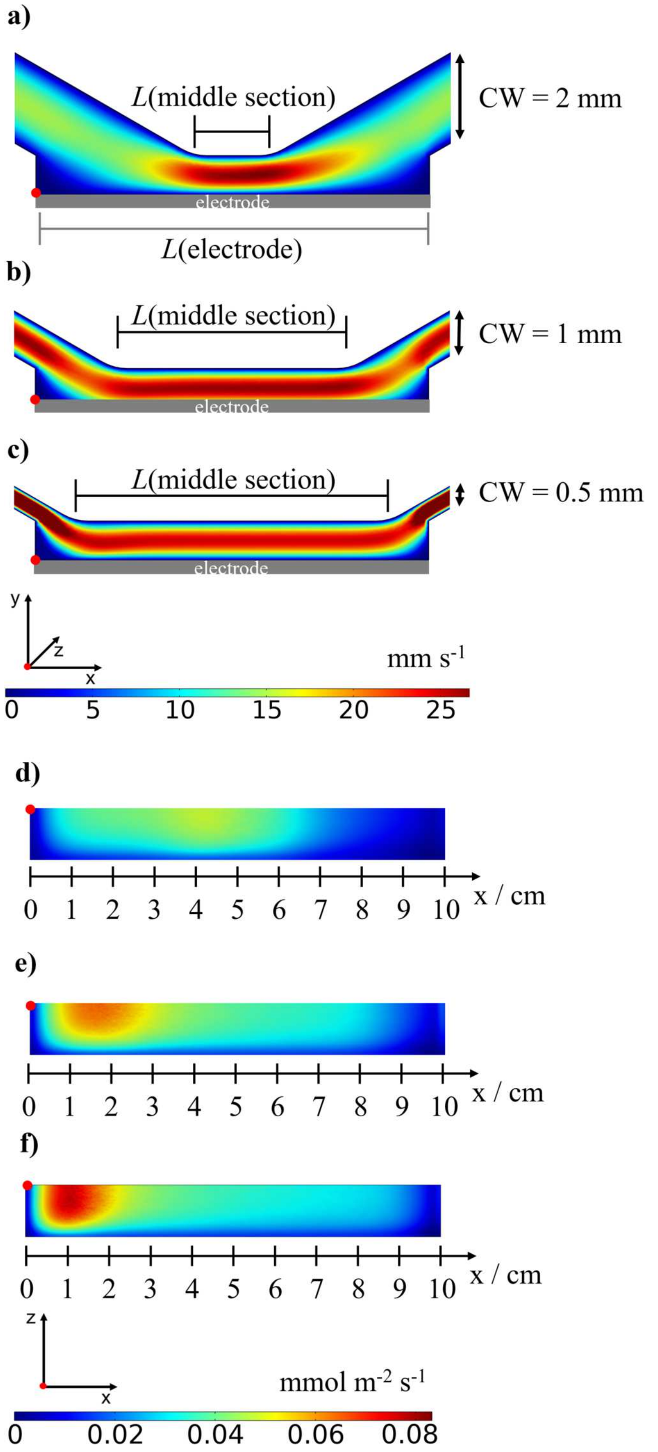

**Figure 5.** Flow velocity distribution at the central x-y plane (a, c, e) and species flux distribution at the electrode (b, d, f) in the mass-transport-limited regime for a CW of 2 mm (a, b), 1 mm (c, d) and 0.5 mm (e, f). The inlet volume flow is 1.14 mL $\text{min}^{-1}$ (for half of the inlet's cross-section), and the overpotential is 1.5 V. The channel height is 1 mm, and the cell width is 2.5 mm (symmetry plane at 1.25 mm). The scale ranges from 0–27 mm $\text{s}^{-1}$ (a, c, e) and 0–83.3 μmol $\text{m}^{-2}$ $\text{s}^{-1}$ (b), (d), (f).

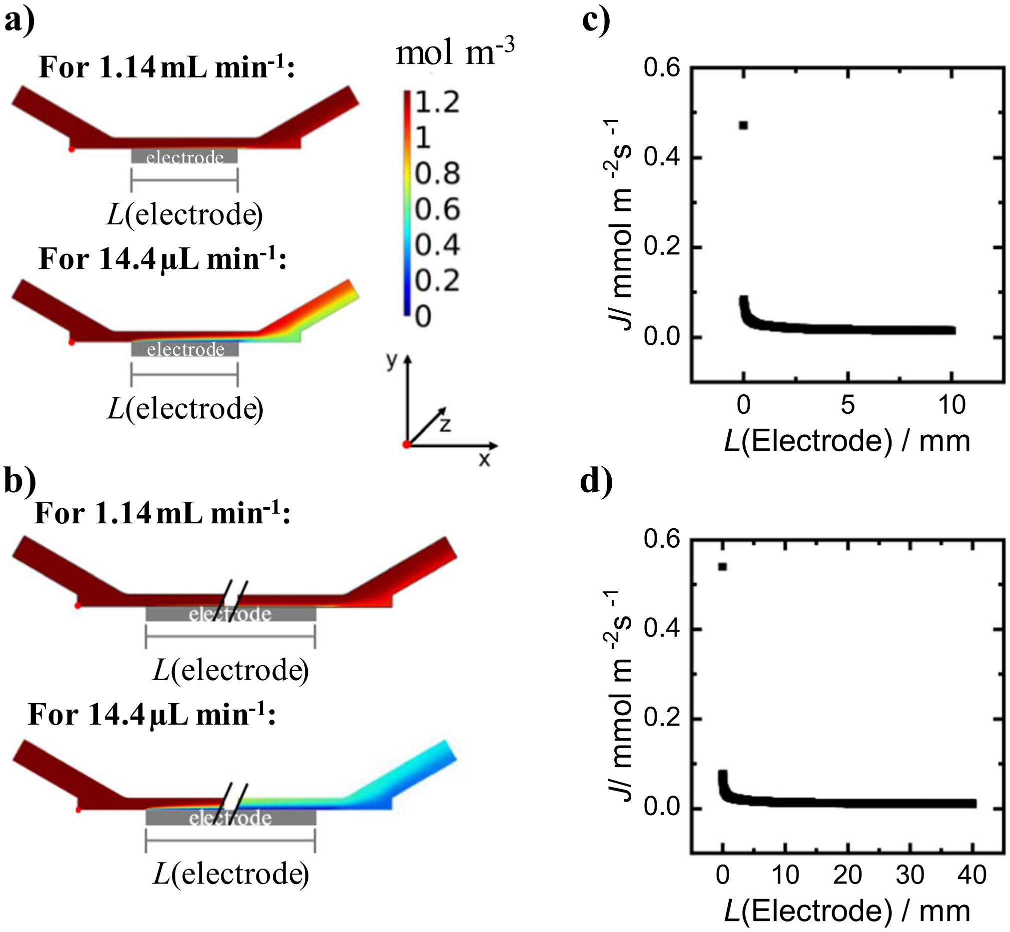

**Figure 6.** Concentration distribution at the central x-y plane (a, b) and species flux distribution at the electrode (c, d) in the mass-transport-limited regime for a 1 cm (a, c) and 4 cm (b, d) long electrode. The inlet flow rate is 1.14 mL $\mathrm{min}^{-1}$ (for half of the inlet's cross-section). For better visualization, the concentration distribution in a) and b) is also shown for an inlet volume flow rate of 14.4 μL $\mathrm{min}^{-1}$. The respective $G$ values are 1% ($L$(electrode) = 1 cm) and 3% ($L$(electrode) = 4 cm). The channel height is 1 mm, and the cell width is 2.5 mm (symmetry plane at 1.25 mm). The overpotential is 1.5 V. The scale ranges from 0–1.26 mol $\mathrm{m}^{-3}$ (a–b). Note that the slight deviation of the maximum species flux at the central x-y plane between the 1 cm (c) and 4 cm (d) long electrode is an artifact of the simulation as the simulation mesh is different for each geometry and, therefore, the data points do not necessarily coincide.

distribution and species flux clearly reflect the expected gradual stabilization of the diffusion layer along the electrode. It is interesting to point out that this species flux profile shows similarities to the one from the SFC (compare Fig. 3c), where the species flux is also strongly influenced by the diffusion layer growth along the electrode.

The KL analysis identified deviations of $i_{\mathrm{kin,sim}}$ from $i_{\mathrm{kin,input}}$ of 1% for 1 cm and 3% for 4 cm long electrodes. Comparing this to the $G$ values discussed above, this indicates that uniform accessibility can be neglected for our pEFC when investigating the reaction kinetics. In comparison to the variation of convection, the variation of the electrode length has a less significant impact on $G$.

***Final pEFC design.***—For our pEFC design, these two investigations on the mass transport of reactive species to the electrode (flow velocity distribution over the WE, uniform accessibility) highlight that the WE needs to be placed in the middle-section between the channels for a uniform flow profile over the WE and for the deviation of $i_{\mathrm{lim}}$ over the WE to be negligible. With the WE in the middle section, the influence of the non-uniform accessibility on the KL analysis was found to be negligible for 1–4 cm long electrodes. When combining the pEFC with downstream analysis, which is limited in the flow velocity, the electrode's width is limited to obtain sufficiently high flow velocities over the WE and, thus, high species fluxes. Because of this, and for practicality in handling, an electrode size of 1 × 1 cm was chosen.

The final flow geometry of the pEFC with a 1 × 1 cm WE in the connecting middle section was simulated, as shown in Fig. 7. Here, the geometry (a) and the simulation results for the velocity distribution (b) and concentration distribution (c) at the central x-y plane of the cell and the species flux over the electrode (d) are shown. The flow velocity distribution in Fig. 7a shows a laminar flow through the channel with dead zones in the transition areas between the in-/outlet channel and the middle-section. It proves the uniform flow profile over the WE when the WE is placed in the middle-section. Thus, the concentration distribution (c) at the central x-y plane of the cell and the species flux over the electrode (d) in Fig. 7 reflect only the effect of the non-uniform accessibility of the electrode, similar to the results seen in Fig. 6. This means that the reactants deplete along the electrode and the diffusion layer thickness increases. Still, the deviation of $i_{\mathrm{kin,sim}}$ from $i_{\mathrm{kin,input}}$ ($G$ value) is quite low for this design. The simulated $G$ value is 2%, and the average species flux over the electrode is 23 μmol $\mathrm{m}^{-2}$ $\mathrm{s}^{-1}$, which gives the smallest deviation of $i_{\mathrm{kin,sim}}$ from $i_{\mathrm{kin,input}}$ and the largest kinetic regime for the 1-$\mathrm{cm}^2$-models presented herein.

These simulations prove that, with the herein-designed pEFC, a precise activity determination of electrocatalysts is possible over a wide potential range, while featuring an industrially more relevant cell geometry. In contrast to the previously reported online-coupled EFCs, this pEFC obtains larger, parallel electrodes and a parallel electrolyte flow over the electrodes. By this, the geometry of the pEFC is one step closer to the industrial scale. Mimicking the industrial cell configuration already at these small scales is vital as it can alter mass transport to the electrode, product distributions, electrode performances and stability. However, it needs to be pointed

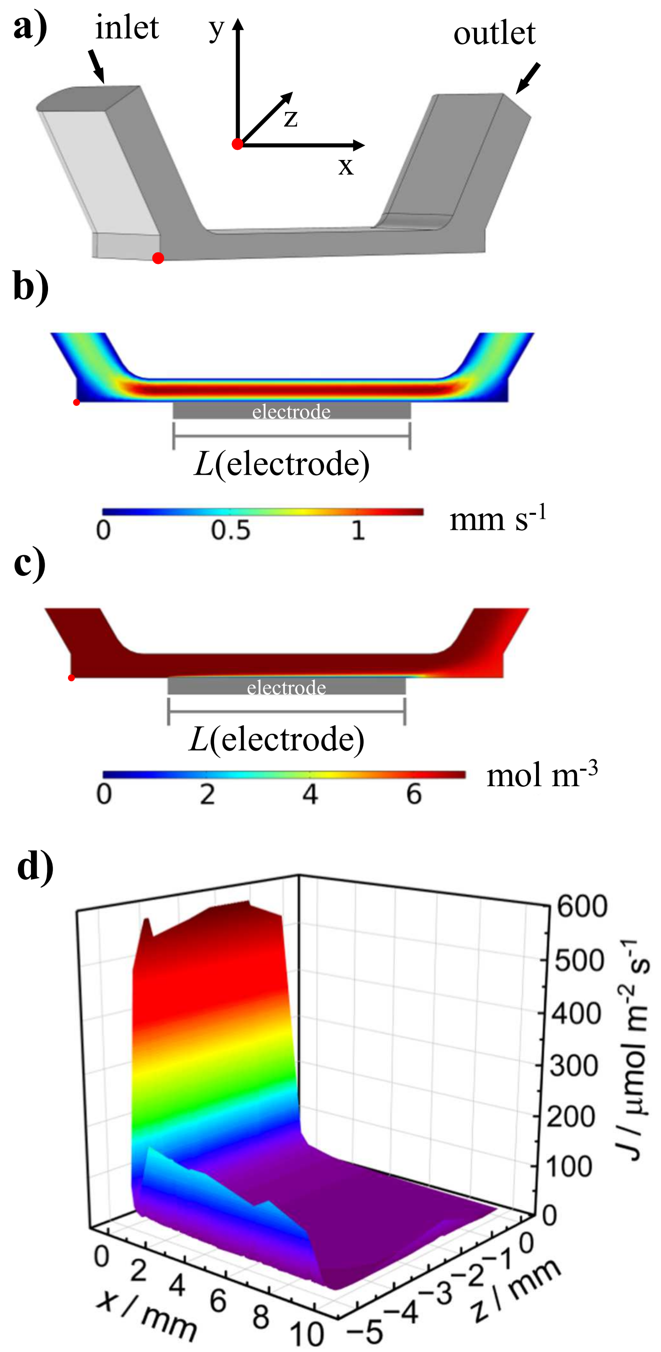

**Figure 7.** (a) Flow geometry of the final flow cell design, (b) flow velocity distribution at the central x-y plane, (c) concentration distribution at the central x-y plane, and (d) species flux distribution at the electrode. The inlet volume flow is 1.45 mL $min^{-1}$ (for half of the inlet's cross-section), and the overpotential is 1.5 V. The channel height is 1 mm, and the cell width is 10 mm (symmetry plane at 5 mm). The scale ranges from 0–1.26 mol $m^{-3}$ (b) and 0–7.01 mm $s^{-1}$ (c). The simulated $G$ value is 2%, and the average species flux over the electrode is 23 μmol $m^{-2}$ $s^{-1}$.

out that with the application of these parallel electrodes cross-contamination from CE processes on the WE and *vice versa* cannot be excluded. Hence, always the full system needs to be considered, and the effect of a potential cross-over should be carefully evaluated. For example, the type of CE and CE reaction should be chosen carefully. A CE that is inert under the reaction conditions is advisable to minimize electrode dissolution. Further, if only non-gas-evolving reactions are studied and, thus, the flow remains laminar, the flow rate can be adjusted to avoid a mixing of the diffusion layers at the electrodes, minimizing the cross-contamination. Alternatively, the distance between the electrodes can be increased to further separate the anode and cathode reaction, keeping in mind that mass transport limitation will then begin earlier. Future work could focus on enabling the integration of a separator into this design.

Note that the channel angle to the x-z plane should not affect mass transport to the electrode and can be varied between 30°–90°, since the WE is placed in the middle section of the flow cell, where parallel flow with a uniform distribution is given. For constructive reasons, a minimum of 30° is needed for a channel height of 1 mm over the WE. By increasing the angle between the channel and the bottom x-z plane, the dead zones at the edges increase. This might result in an accumulation of reactants and products incl. gases in these regions. While an accumulation of the reactants in the edges might generally challenge the precise online monitoring of the electrolyte, especially gas accumulations can be problematic. The latter can hinder the electrolyte flow or even block the electrode when gas accumulation becomes excessive.

***Experimental validation.***—Based on these theoretical simulations, the flow velocity distribution, concentration distribution, and species flux of the final pEFC flow geometry were validated experimentally. For that purpose, the applicability of the Levich analysis and the KL relationship was tested by recording polarization curves at different flow velocities for the ferricyanide reduction. The respective polarization curves can be found in Fig. S-5. The results for the Levich analysis and the KL plot in the mixed kinetic-mass-transport regime at a potential of 0.593 V *vs* RHE can be seen in Fig. 8 for four different repetitions (V1-V4). It must be noted that the potential regime for the applicability of the KL analysis to the ferricyanide reduction is very narrow due to its fast reaction kinetics.

The Levich analysis (a) and the KL plots (b) in Fig. 8 show a linear relationship with an averaged slope of 0.39 ± 0.03 and 0.96 ± 0.02, respectively. From the KL plots in Fig. 8b, $|1/I_{kin}|$ (y-intercept) of 0.37 ± 0.07 can be identified, corresponding to a kinetic current of 2.7 ± 0.3 mA. The slight variations between the different repetitions in Figs. 8a and 8b) might be associated with different $[Fe(CN)_6]^{3+}$ concentrations present in the electrolyte as the solution was not long-term stable. $[Fe(CN)_6]^{3+}$ is protonated in 0.1 M $HClO_4$ and the decay depends strongly on the electrolyte concentration, acid concentration, temperature, impurities and available light.[23] Another source of error could be the varying precision of the flow rates because of their high sensitivity to hydrostatic pressure, i.e. to the electrolyte level in the reservoir, the position of the tubing and the pEFC, and the influence of the pump. To get an understanding of how these parameters influence the limiting current, we performed an uncertainty propagation based on the theoretical Levich equation (see SI). It becomes clear that the 3D-printing precision has the most significant impact on $I_{lim}$ followed by the concentration and the flow rate variation, assuming that always a new cell is used for each experiment. Even if the same cell would be used, variations in the channel height might still occur by variations in the tightening pressure and age of the sealing O-ring. The total uncertainty of $I_{lim}$ according to the uncertainty propagation is 2.9%. Still, the overall reproducible linearity of the Levich analysis and the KL relationship, in combination with a slope close to one for the KL plot, substantiates the applicability of the Levich analysis and KL relationship for this cell design. The 4% deviation of the KL slope from one is in line with previous reports, suggesting a systematic deviation between uniform accessible electrodes and electrodes in EFCs.[6,13] The KL analysis in Fig. 8b additionally demonstrates that the kinetics of a catalyst can be evaluated in the mixed kinetic-mass-transport regime with this pEFC.

***Relative electrode positioning.***—While designing, simulating, and experimentally validating this pEFC with a 1 $cm^2$ WE, the relative electrode positioning of WE, CE, and RE was found to be of great importance and significantly influenced the electrochemical

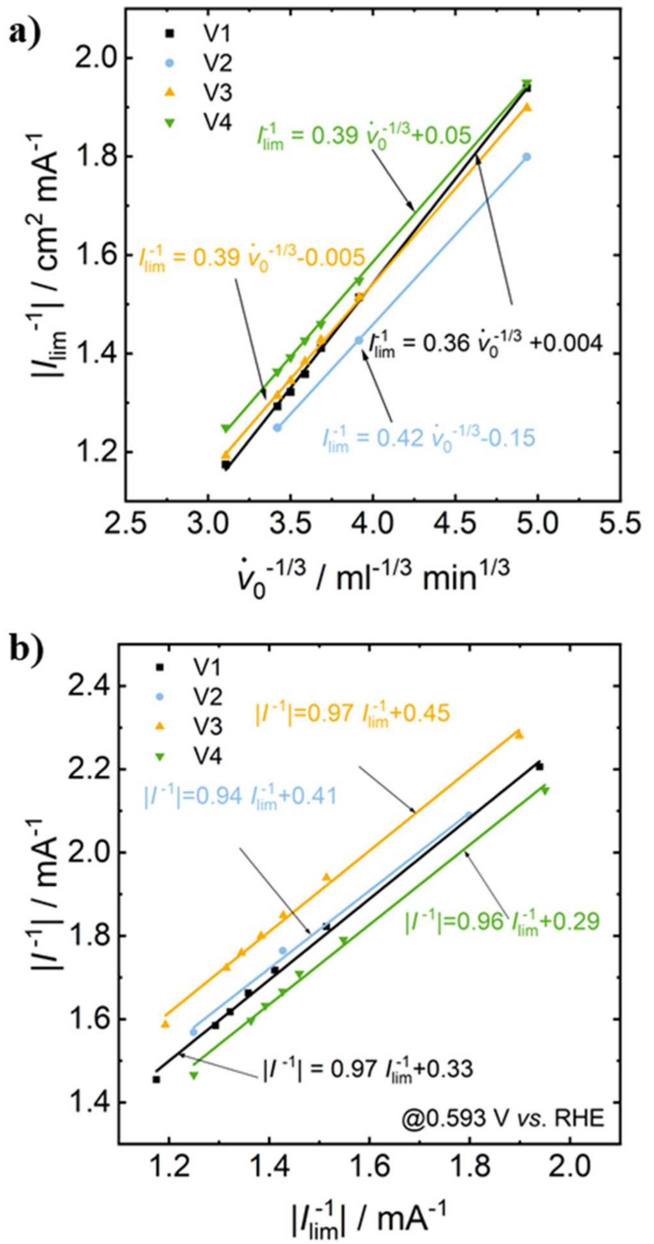

**Figure 8.** (a) Experimental Levich analysis and (b) KL plot for the ferricyanide reduction in 0.1 M $HClO_4$ with 10 mM $K_3[Fe(CN)_6]$ in the final pEFC design with repetitions 1–4 (V1-V4). The KL plot was evaluated at an overpotential of 0.593 V *vs* RHE. The inlet volume flow was varied between 0.5–2 mL min$^{-1}$. The Levich and KL relationship proved to be applicable for the herein-designed pEFC with a KL slope of 0.96 ± 0.02.

measurement, primarily high-frequency measurements such as EIS. Thus, three different geometries, as seen in Fig. 9, were investigated to identify the dominating effects for successful EIS in EFCs where the electrodes are separated by narrow and winded channels. In all cases, the RE was connected to the inlet by a capillary with a diameter of 1 mm.

For the herein-developed flow geometry of the pEFC, two electrode configurations are theoretically plausible: parallel WE and CE (Fig. 9a) or the CE as a rod in the outlet (Fig. 9b). While parallel WE and CE are standard in the industry, the CE is, however, favored in the outlet in analytical electrochemistry to avoid contaminations at the WE. The V-EFC was additionally tested for more insight (Fig. 9c). In all cell designs, the WE is positioned at the bottom.

When performing EIS measurements for the three different setups shown in Fig. 9, EIS was only successful for the parallel electrode arrangement (Fig. 9a) and the original V-EFC (Fig. 9c). The respective Bode plots can be seen in Fig. S-6. This might be due to the homogeneous current distribution at the WE and a convenient point of potential measurement by the capillary of the RE. The capillary of the RE, here, presumably detects homogeneous equidistant and parallel potential lines between WE and CE. For the pEFC design in Fig. 9b, the suggested region of parallel and uniform current lines between CE and WE is spatially separated from the region of potential measurement by the RE. This is illustrated in Fig. S-7, which shows the potential distribution within the channels at a cell potential of 10 mV. The wide, inhomogeneous spacing of the equipotential lines near the RE position, where the potential is sensed, indicates a weak potential field in this region. Since the potentiostat regulates the current between WE and CE to achieve the target potential at the RE, the actual potential difference between WE and CE must become much larger to enable an intensified potential field at the RE. This effect is particularly pronounced in our system, as the narrow flow channels lead to a considerable iR drop between WE and CE, requiring the application of correspondingly higher currents, and, thus, potentials, to maintain the desired potential at the RE. During PEIS, the dynamically requested potential between WE and RE is, thus, not established quickly enough, leading to control amplifier overloads, which ultimately prevent reliable PEIS measurements.

To summarize, electrodes in EFCs with narrow and winded channels need to be placed in a way that a uniform current distribution over the WE is possible and that the RE can sense parallel, equidistant, and uniform potential lines. Practically, this means that the projection of the RE's capillary onto the WE needs to intersect with a region of parallel and equidistant current and potential lines between CE and WE. This is also in line with previous reports.[24–26]

***Online electrolyte monitoring during alkaline water electrolysis.***—Utilizing the V-EFC design, Spanos et al. proposed the coupling of an online-coupled EFC and ICP-OES as a technique to characterize simultaneously a catalyst's activity and stability for the AWE, more specifically for the OER. Although not yet widely used, this technique of coupling an online-coupled EFC and ICP-OES to study AWE electrocatalysts is very promising as it can address the discrepancy between high activity and low stability. In particular, the stability of the electrocatalyst is of crucial importance for industrial application, and therefore, an in-depth understanding of the deactivation mechanisms is required.[5] These could be elucidated with the help of online ICP-OES. As a consequence, the herein-developed pEFC should be adaptable to the needs of studying AWE electrocatalysts at lab- (up to 10 mA cm$^{-2}$, RT, 1 M KOH) and industrially more relevant (up to 100 mA cm$^{-2}$, 80 °C, 30 wt% KOH) conditions. When applying industrially more relevant conditions, additional challenges arise such as increased gas evolution, including possible electrode blockage or trapped gas bubbles, and the cell's material stability toward highly concentrated alkaline electrolytes and high temperatures.

Regarding material stability, AR-H1 (Keyence) as 3D-printing material and EpoHeat Clear (Buehler) as embedding material were identified as suitable for 30 wt% KOH and 80 °C. One requirement was that the material is transparent to see and react to trapped gas bubbles. Further, sufficient resolution of 20 μm[20] and a manufacturing tolerance of 0.1 mm[27] (Polyjet technology) were to be ensured, and no weight loss, embrittlement, deformation, or visual change should occur. The effect of gas bubbles on the activity determination can be clearly seen in Fig. S-8a by the unsteady CP at 10 and 100 mA cm$^{-2}$. This effect is quantified by calculating the average absolute deviation between the linear regression and the measured potential over the duration of the experiment. For 10 mA cm$^{-2}$, this deviation ($E_{osc}$) amounts to 2.3 mV, whereas for 100 mA cm$^{-2}$ the value was not determined because the cell flooded with gas bubbles, causing an exorbitant potential increase. To achieve a more efficient gas removal, the interelectrode distance was increased to 3 mm, the angle between the in- and outlet channel

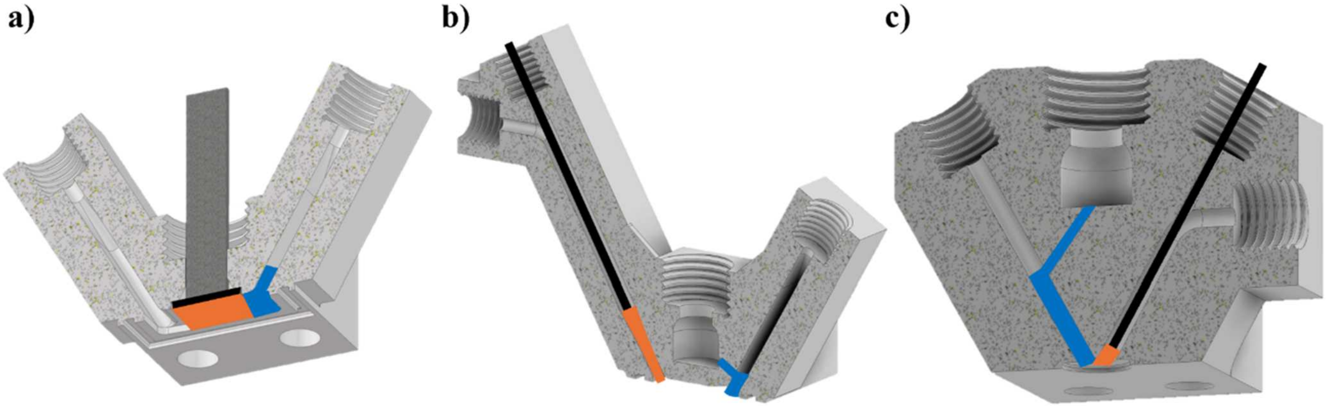

**Figure 9.** Schematic illustration of the RE capillary (blue) and the suggested regions of equidistant parallel potential lines between WE and CE (orange) for different electrode positionings in EFCs with narrow and winded channels. The WE is positioned at the bottom. (a) Herein-designed pEFC with parallel WE and CE electrodes, (b) herein-designed pEFC with the CE in the outlet as a rod, (c) V-EFC with the CE in the outlet as a rod.

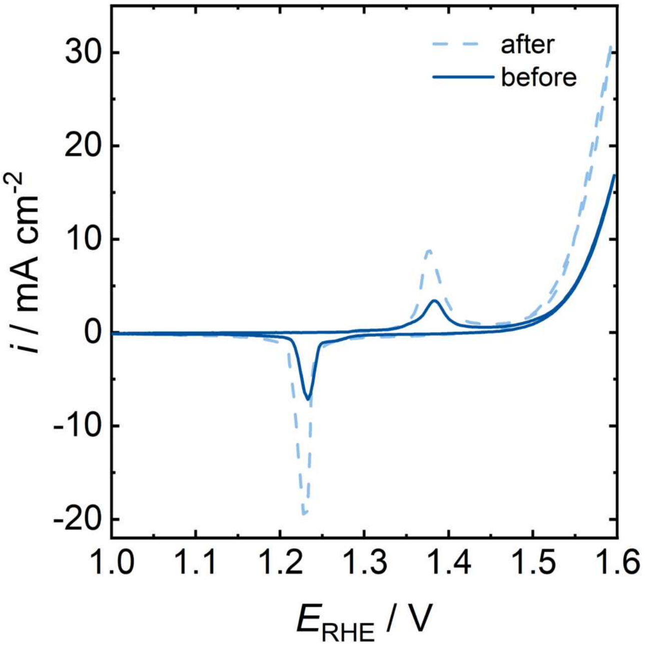

**Figure 10.** CV (1–1.6 V, 100 mV $s^{-1}$) for a $Ni_{99.99}$ electrode, measured in 30 wt% KOH and 80 °C in the herein-designed pEFC before and after electrochemical conditioning of the electrode. CV conditioning was performed between 0.5–1.6 V at 100 mV $s^{-1}$ for 30 min in 30 wt% KOH at 80 °C. An electrochemical activation from conditioning is visible.

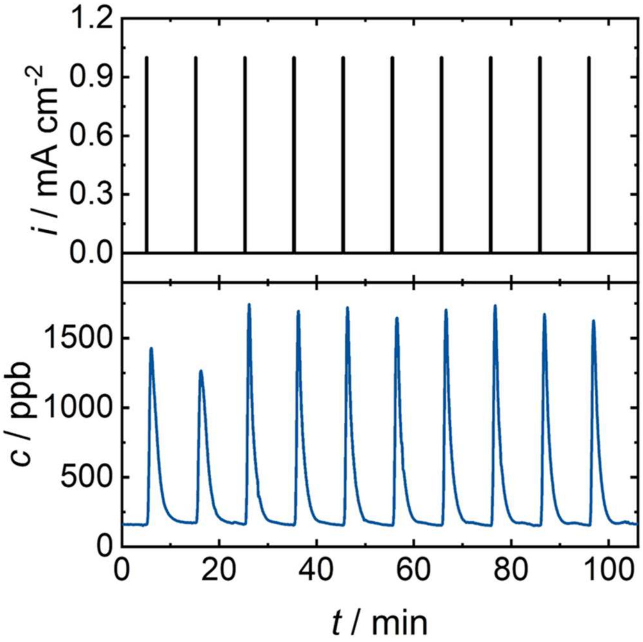

**Figure 11.** Ni dissolution in Ar-purged 0.1 M $HClO_4$ from a $Ni_{99.99}$ anode, when applying a series of 10 CPs at 1 mA $cm^{-2}$ for 10 s w *i*th a delay of 10 min between each CP. A glassy carbon CE was used, and a flow rate of 1 mL $min^{-1}$ was applied. The experiment was conducted at room temperature.

and the bottom was minimized to 30°, and the middle section was prolonged, increasing the distance between CE and the outlet channels. It needs to be considered that increasing the interelectrode distance raises the dilution of the reaction and electrode dissolution products, which could become problematic for their detection by the ICP-OES. Further, the fluid velocity over the WE is decreased. This would correspond to an increased mass transport limitation, which is, however, a) counteracted by the turbulence introduced by the gas evolution and b) not relevant for the OER due to the high availability of hydroxide ions (i.e., reactants). The adapted design to study AWE electrocatalysts is depicted in Fig. 1b and Fig. S-8b. By these adaptations, a stable CP measurement to determine the OER activity at up to 100 mA $cm^{-2}$ is obtained (Fig. S-8b, $E_{osc}$ of 0.2 mV and 0.4 mV for 10 and 100 mA $cm^{-2}$, respectively). Further, electrochemical measurements such as CV and CP at 10 and 100 mA $cm^{-2}$ can now also be performed in 30 wt% KOH at 80 °C, as can be seen in Fig. 10 (CV) and Fig. S-9 (CP). Figure 10 shows two CVs for a $Ni_{99.99}$ electrode in 30 wt% KOH at 80 °C before and after it was conditioned. Conditioning was conducted between 1–1.6 V at 100 mV $s^{-1}$ for 30 min. Here, the $Ni(OH)_2$/NiOOH redox peaks are clearly resolved as well as the exponentially increasing OER current. After conditioning, the $Ni(OH)_2$ layer and OER activity are increased. This enlarged $Ni(OH)_2$ layer likely contributes to the enhanced activity, which is consistent with observations from our previous work, where the impact of electrochemical conditioning on electrode performance is discussed in more detail. [21]

Lastly, the applicability of coupling the AWE-pEFC to the ICP-OES for online monitoring of the electrolyte during electrochemical operation was tested. For that, the Ni dissolution from a Ni electrode ($Ni_{99.99,}$ 99.99 wt% Ni) in 0.1 M $HClO_4$ was first measured as a reference. CP pulses were applied, and their starting time was correlated with the onset time of the Ni dissolution peak, aligning the electrochemical and spectroscopic timescale. Figure 11 shows the Ni concentration when applying the series of 10 CPs at 1 mA $cm^{-2}$ for 10 s separated by a 10 min delay. In Fig. 11, the first two peaks differ in peak shape and area slightly from the following eight peaks,

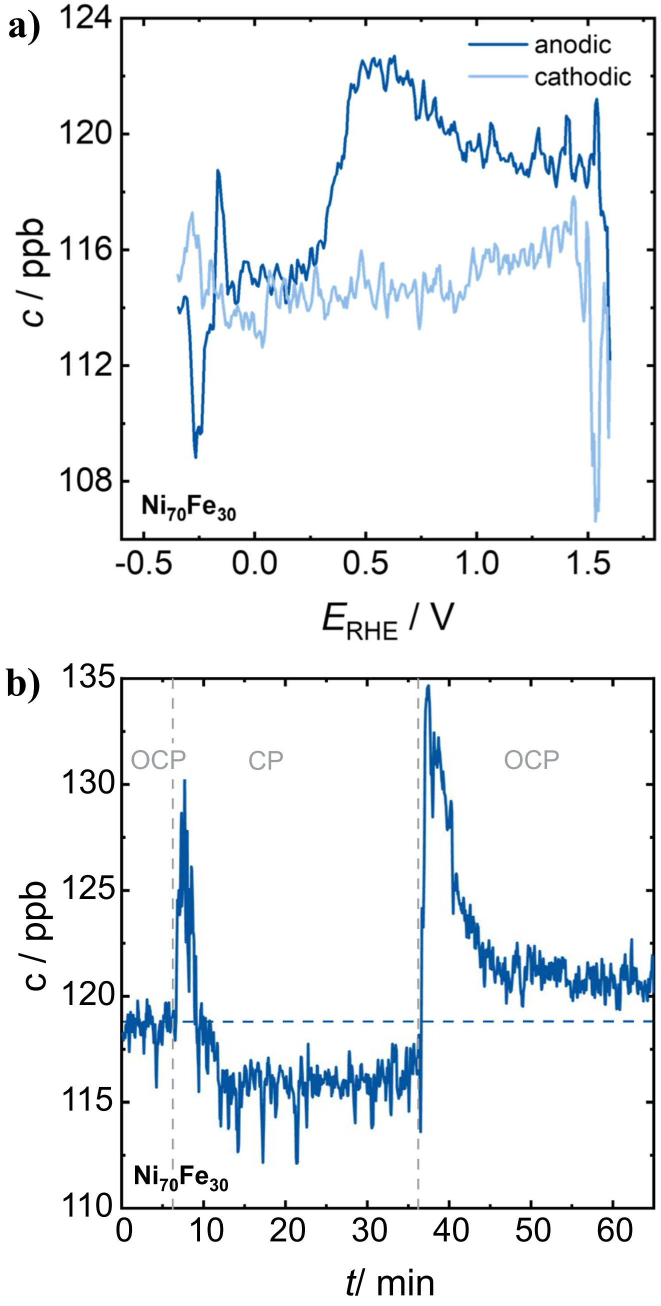

**Figure 12.** (a) Fe concentration, measured by ICP-OES, during CV between –0.35–1.6 V at 2 mV $s^{-1}$. (b) Fe concentration, measured by ICP-OES, during the application of, first, a 30-min CP at 10 mA $cm^{-2}$ and then, a 30-min OCP measurement. A 1 $cm^2$ $Ni_{70}Fe_{30}$ electrode was used as an anode and glassy carbon as a cathode. Data was cleaned from spikes to low concentrations due to gas evolution (no trends were modified) and was smoothed over 3 data points. Experiments were conducted in 1 M KOH at room temperature. [Fig. 12a reprinted with permission of John Wiley and Sons[21]].

suggesting an initial equilibration. Disregarding the first two peaks and averaging over the remaining eight peaks, the maximum of the Ni dissolution peak follows the current pulse with a delay of 50 ± 4 s. The concentration drops back to the initial concentration and reaches it after approx. 4.0 ± 0.3 min. These times need to be considered when interpreting future ICP-OES results with the herein-designed pEFC. In literature, the concentration decline to the baseline was reported to be between 4–5 min when using the SFC.[3,28,29] This demonstrates that the herein-designed pEFC is suitable for studying electrode stability and dissolution despite the larger electrode area and the cell design with more dead zones and transitions.

In the next step, the potential- and time-dependent dissolution of a Ni-Fe alloy anode with 30 wt% Fe ($Ni_{70}Fe_{30}$) in 1 M KOH was studied. Two different studies were performed: a) CV between –0.35–1.6 V *vs* RHE at 2 mV $s^{-1}$ (Figs. 12a and 12b) CP at 10 mA $cm^{-2}$ for 30 min, followed by 30-min OCP (Fig. 12b). Figure 12a shows the potential-dependent dissolution of Fe from $Ni_{70}Fe_{30}$ during CV for the oxidative and reductive sweep. Sharp signal drops can be seen at the HER (<–0.1 V) and OER (>1.5 V) potentials. This might be because of a decrease in electrolyte supply to the ICP-OES due to gas bubbles. From the baseline of 115 ppb Fe, the Fe concentration starts to increase at 0.2 V *vs* RHE during the anodic sweep. At 0.55 V, it reaches its maximum of 123 ppb, and the Fe concentration decreases afterward to 119 ppb at 1.3 V. On the cathodic sweep, the Fe concentration drops linearly to the initial Fe concentration. Figure 12b shows the time-dependent Fe dissolution from a $Ni_{70}Fe_{30}$ anode during CP at 10 mA $cm^{-2}$, followed by OCP. Here, the initial Fe concentration is about 119 ppb. A sharp increase in Fe concentration to 130 ppb is visible when applying 10 mA $cm^{-2}$, followed by a drop to 116 ppb. After the CP ends and the potential is reversed to OCP, the Fe concentration spikes to ∼135 ppb and, then, equilibrates to 120 ppb. This suggests an initial Fe dissolution from $Ni_{70}Fe_{30}$, which is followed by an Fe uptake at the anode or cathode during the CP. A simultaneous dissolution from the $Ni_{70}Fe_{30}$ anode cannot be excluded. After the CP, the Fe seems to be released again. The noise probably results from the rather high KOH concentrations and gas bubble interferences. Overall, Fig. 12 proves the possibility of deconvoluting metal dissolution from AWE electrocatalysts or metal incorporation from the electrolyte in 1 M KOH at room temperature.

## Conclusions

In this work, we designed an EFC with a 1 $cm^2$ WE for simultaneous activity measurement and downstream analysis of the electrolyte. COMSOL simulations of the flow velocity, concentration distribution, and species flux distribution were performed to evaluate different cell geometries.[6] Simulations of the scaled-up versions of the previously reported SFC from Mayrhofer et al.[4,6] and V-shaped EFC from Schlögl et al.[5] identified a limited kinetic regime and formation of large dead zones, respectively. Our designed pEFC features parallel 1 $cm^2$ electrodes, and a uniform, laminar flow over the WE. It, therefore, resembles more closely an industrial flow cell configuration. For a minimal dilution of the reaction products and maximized flow velocity over the WE, the reaction volume over the WE was minimized by tilting the in- and outlet channels with an angle of 30–90° to the x-z plane. A laminar flow, which is parallel to the electrodes and uniform over the WE, is ensured by placing the electrode in the middle of the connecting channel. Thereby, the precision in activity determination is maximized. For our pEFC, we further showed that the uniform accessibility of the electrode can be neglected for an electrode length of less than 4 cm when calculating the activity *via* the KL relation. The simulation of the final pEFC cell design revealed a $G$ value of 2% for the determination of $i_{\text{kin}}$. This indicates that the KL analysis can be applied here with high accuracy. The applicability of the Levich equation and the KL relationship was validated experimentally for the ferricyanide reduction.

For accurate potential determination with interfering gas evolution when studying AWE electrocatalysts, we adjusted the pEFC design. The angle between the in- and outlet channel to the bottom (x-z plane) was minimized to 30°, the middle section was prolonged, and the distance between WE and CE was increased. Coupling the pEFC to ICP-OES, the Fe concentration was successfully monitored during CV and CP at 10 mA $cm^{-2}$ with a $Ni_{70}Fe_{30}$ anode in 1 M KOH at room temperature.

With the herein-designed pEFC, the activity and stability of newly developed catalysts can now be characterized under industrially more relevant conditions with parallel 1 $cm^2$ electrodes and a parallel and uniform flow velocity distribution. This pEFC enables a deeper and more application-oriented understanding of why electrocatalysts often have high activity but low stability, enhancing the transition of electrocatalysts from academia to industry.

## Acknowledgments

We acknowledge financial support from the German Federal Ministry of Research, Technology and Space (BMFTR project “PrometH2eus,” FKZ 03HY105A). Simulations were performed with computing resources granted by RWTH Aachen University under the project IDs 4708 and 4967. Simulation software was provided by the Chair of Chemical Process Engineering at RWTH Aachen University. We thank Victor Schulte for his valuable contributions to the study of relative electrode positioning in the electrochemical flow cells. Further, many thanks to N. Röttcher (group of K. J. J. Mayrhofer, Helmholtz-Institute Erlangen-Nürnberg) for the valuable discussions and the 3D-printing material samples.

## Data Availability

The Supporting Information to this article can be found on the journal's website. The data set corresponding to this article is published under DOI 10.5281/zenodo.17775585.

## ORCID

C Gohlke https://orcid.org/0009-0006-8273-6354
C Marcks https://orcid.org/0000-0003-3618-4246
V Seidl https://orcid.org/0000-0003-3310-700X
M Padligur https://orcid.org/0000-0002-5234-9031
A K Mechler https://orcid.org/0000-0002-0491-514X

## References

1. S. Chu and A. Majumdar, *Nature*, **488**, 294 (2012).
2. Z.-P. Wu, X. F. Lu, S.-Q. Zang, and X. W. Lou, *Adv. Funct. Mater.*, **30**, 1910274 (2020).
3. O. Kasian, S. Geiger, K. J. J. Mayrhofer, and S. Cherevko, *Chem. Rec.*, **19**, 2130 (2019).
4. A. K. Schuppert, A. A. Topalov, I. Katsounaros, S. O. Klemm, and K. J. J. Mayrhofer, *J. Electrochem. Soc.*, **159**, F670 (2012).
5. I. Spanos, A. A. Auer, S. Neugebauer, X. Deng, H. Tüysüz, and R. Schlögl, *ACS Catal.*, **7**, 3768 (2017).
6. N. Kulyk, S. Cherevko, M. Auinger, C. Laska, and K. J. J. Mayrhofer, *J. Electrochem. Soc.*, **162**, H860 (2015).
7. A. J. Bard and L. R. Faulkner, *Electrochemical Methods: Fundamentals and Applications* (Wiley, New York) (2001).
8. N. Thissen, J. Hoffmann, S. Tigges, D. A. M. Vogel, J. J. Thoede, S. Khan, N. Schmitt, S. Heumann, B. J. M. Etzold, and A. K. Mechler, *ChemElectroChem*, **11**, e202300432 (2024).
9. J. A. Cooper and R. G. Compton, *Electroanalysis*, **10**, 141 (1998).
10. V. M. Schmidt, *Elektrochemische Verfahrenstechnik* (Hoboken)(Wiley-VCH) (2012).
11. N. Wakabayashi, M. Takeichi, M. Itagaki, H. Uchida, and M. Watanabe, *J. Electroanal. Chem.*, **574**, 339 (2005).
12. G. R. Engelhardt, R. Biswas, Z. Ahmed, S. N. Lvov, and D. D. Macdonald, *Electrochim. Acta*, **52**, 4124 (2007).
13. D. A. Scherson, Y. V. Tolmachev, Z. Wang, J. Wang, and A. Palencsar, *Electrochem. Solid-State Lett.*, **11**, F1 (2007).
14. S. E. Temmel, S. A. Tschupp, and T. J. Schmidt, *Rev. Sci. Instrum.*, **87**, 45115 (2016).
15. J. P. Kollender, M. Voith, S. Schneiderbauer, A. I. Mardare, and A. W. Hassel, *J. Electroanal. Chem.*, **740**, 53 (2015).
16. T. F. O’Brien, T. V. Bommaraju, and F. Hine, *Handbook of Chlor-Alkali Technology: Volume I: Fundamentals* (Springer, New York) (2005).
17. A. Godula-Jopek, *Hydrogen Production by Electrolysis* (Weinheim, Germany) (Wiley-VCH) (2015).
18. R. G. Compton and P. R. Unwin, *J. Electroanal. Chem. Interfacial Electrochem.*, **205**, 1 (1986).
19. G. D. O’Neil, S. Ahmed, K. Halloran, J. N. Janusz, A. Rodríguez, and I. M. Terrero Rodríguez, *Electrochem. Commun.*, **99**, 56 (2019).
20. K. Deutschland GmbH, (2020), Hochauflösender 3D-Drucker Modellreihe AGILISTA-3000 https://www.keyence.de/mykeyence/?ptn=001&ad_local=modelcat.
21. C. Gohlke, J. Gallenberger, N. Niederprüm, H. Ingendae, J. Kautz, J. P. Hofmann, and A. K. Mechler, *ChemElectroChem*, **11**, e202400318 (2024).
22. C. Gohlke, J. Gallenberger, N. Niederprüm, H. Ingendae, J. Kautz, J. P. Hofmann, and A. K. Mechler, (2025) *Dataset for Publication: Boosting the Oxygen Evolution Reaction Performance of Ni-Fe-Electrodes by Tailored Conditioning*, Zenodo.
23. P. L. Domingo, B. García, and J. M. Leal, *Can. J. Chem.*, **68**, 228 (1990).
24. S. Barnartt, *J. Electrochem. Soc.*, **108**, 102 (1961).
25. S. Barnartt, *J. Electrochem. Soc.*, **99**, 549 (1952).
26. J. E. Harrar and I. Shain, *Anal. Chem.*, **38**, 1148 (1966).
27. rapidobject GmbH, (2023), Fertigungstoleranzen https://www.rapidobject.com/downloads/#zu-beachten.
28. L. Rossrucker, K. J. J. Mayrhofer, G. S. Frankel, and N. Birbilis, *J. Electrochem. Soc.*, **161**, C115 (2014).
29. S. Cherevko, G. P. Keeley, N. Kulyk, and K. J. J. Mayrhofer, *J. Electrochem. Soc.*, **163**, H228 (2016).